



Toward Durable Thermal Barrier Coating with Composite Phases and Low Thermal Conductivity

Xinqing Ma¹ · Kristina Rivellini¹ · Peter Ruggiero¹ · George Wildridge²

Submitted: 13 August 2019 / in revised form: 6 December 2019 / Published online: 22 January 2020
© ASM International 2020

Abstract High-efficiency turbine engines highly rely on the further improvement of the novel technologies related to combustion, cooling and thermal barrier coating (TBC) with the increase in inlet temperatures. Thermal barrier coatings with higher thermal stability and lower thermal conductivity (low- k) than current 8YSZ TBC had attracted a lot of academia and industries' attentions and activities. The present work aimed to focus on exploring a path toward a durable TBC with better thermal durability and low- k capability by overcoming the technical, practical and economic barriers for current low- k TBC development and applications. The concept of composite phase ceramics was proposed for low- k TBC material design, in an effort to combine the desirable attributes of unique phase constitution, low conductivity k , high fracture toughness and good process economy. Further, thermal spray process was optimized for the topcoats of the low- k ceramics by controlling and measuring the effect of key process parameters on porous coating architecture, deposition rate and process efficiency. To evaluate the performance of the low- k TBCs, both an isothermal oxidation test and a thermal cycling test were conducted. The test results of the composite phase

ceramics exhibited promising for a durable low- k TBC measured by several desirable property attributes.

Keywords air plasma spray · low thermal conductivity · oxidation test · composite ceramic · sintering behavior · thermal barrier coating

Introduction

The capability of higher entry operation temperatures and larger thermal gradients is desired for advanced thermal barrier coatings (TBCs) in high-efficiency gas turbine engines. Therefore, there is urgent demand to develop new materials, especially topcoat ceramics with high thermal stability, long durability and low thermal conductivity k (low- k) for the advanced TBCs which are widely used for thermal and environmental protection of superalloy components in the turbine hot sections, such as combustors, fuel nozzles, blades and vanes (Ref 1, 2). The advanced TBCs will allow additional increase in operating temperature without exceeding the limits of the superalloy components and the internal cooling system, and enable continued improvements in engine performance. In view of the fact that superalloys approached their theoretical limits, the development and manufacture of advanced TBCs with low thermal conductivity is critical and vital for new generation turbine engines with significant improvements in fuel efficiency and low emission (Ref 3-5).

From the history of ceramic materials for TBCs, it can be concluded that there is a battle between those desirable properties such as phase stability, thermal conductivity, fracture toughness, durability and cost, as charted in Fig. 1. The initial zirconia-yttria TBC was fully stabilized, containing 12 to 20 wt.% yttria and cubic phase (c), and had

This article is an invited paper selected from presentations at the 2019 International Thermal Spray Conference, held May 26-29, 2019 in Yokohama, Japan and has been expanded from the original presentation.

✉ Xinqing Ma
Xinqing.ma@cwst.com

¹ Surface Technologies Division, Curtiss-Wright Corporation, East Windsor, CT, USA

² IMR Test Labs, Curtiss-Wright Corporation, Lansing, NY, USA

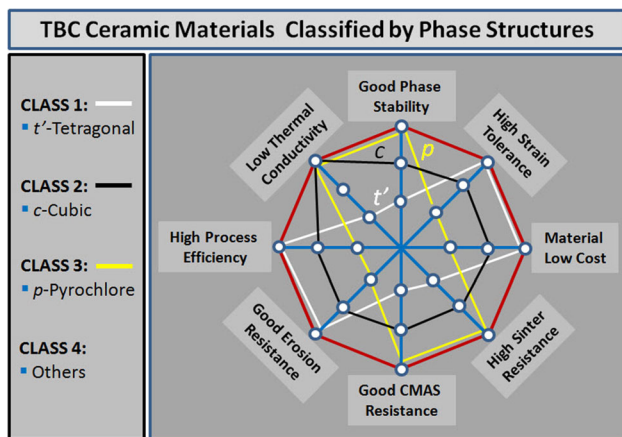


Fig. 1 The challenges for developing new ceramic materials to meet the needs in property, performance, process and economy for the advanced TBCs

good phase stability and low conductivity in the mid 1970 s. Later, it was showed that better ceramic toughness and durability could be achieved by lowering the yttria content to 6–8 wt.% (Ref 6, 7), but scarified phase stability and thermal conductivity. Since then to current date, the ceramic for TBCs is typically 7–8 wt.% yttria partially stabilized zirconia (8YSZ), which has a metastable tetragonal phase (t'), high toughness and a relatively high k 2.0–2.3 W/m K for a fully dense and 0.9–1.2 W/m K for 10–15% porosity at ~ 1000 °C (Ref 8–10).

Many studies and progresses had been made in applying and testing low thermal conductivity ceramics. Two main strategies for the development of promising low- k ceramics had been proposed. One strategy was reported that the co-doping of ZrO_2 with multiple components resulted in lowering thermal conductivity due to cluster formation (Ref 11–13). A solid solution phase, typically cubic phase, was formed in this class of improved zirconia-based ceramics. The examples of thermal barrier coating systems with selected clustered oxides including ZrO_2 - Y_2O_3 - Nd_2O_3 (Gd_2O_3 , Sm_2O_3)- Yb_2O_3 (Sc_2O_3), had reduced thermal conductivity to 0.6–1.1 W/m K at surface temperature ~ 1315 °C, from 1.3–1.4 W/m K for conventional 8YSZ coating. Another strategy was reported that zirconate materials with an $A_2B_2O_7$ -pyrochlore (p) phase structure or an ABO_3 -type perovskite phase structure also resulted in lower thermal conductivity (Ref 14–17). The examples of $A_2B_2O_7$ -pyrochlore oxides include $La_2Zr_2O_7$, $Gd_2Zr_2O_7$ and $Sm_2Zr_2O_7$ with thermal conductivity of 0.9 to 1.55 W/m K.

The low conductivity TBCs will have some significant advantages over a conventional 8YSZ TBC in enabling higher turbine temperatures and power density, improved thermal insulation property, high melting points and high sintering temperature, thin coating thickness, low weight,

good phase thermal stability and low sintering rate. However, some of the challenges to develop new low- k TBCs were discovered (Fig. 1): (1) low thermal durability due to early failure of low- k layer. Cyclic lifetime is compromised with increasing stabilizer content in doped ZrO_2 ; (2) loss of fracture toughness and strain tolerance due to material intrinsic property (Ref 18); (3) low coefficient of thermal expansion (CTE) of zirconates relative to zirconia; (4) potential thermochemical reaction between low- k zirconate ceramics and TGO layer, and thus a 8YSZ interlayer is necessary to prevent the reaction (Ref 19); (5) process conditions for an optimized coating are narrow; (6) high production cost associated with low process efficiency and high price of feedstock material.

This work aimed to address those challenges and technical issues for the development of new class of low- k materials and TBCs. The concept of composite phase ceramics was proposed for low- k TBC material design, in an effort to combine the desirable attributes of unique phase constitution, low conductivity k , high ceramic fracture toughness, superior thermal cyclic durability and good process economy. The test results of the composite phase ceramics revealed promising for a durable low- k TBC measured by several desirable attributes.

Experimental

Topcoat Material Design

With the aim to reduce thermal conductivity and improve thermal cyclic resistance of zirconia-based TBCs, a composite phase material was designed and manufactured. Co-doped zirconia with a cubic phase structure (c) was selected as a primary component for lowering thermal conductivity, and co-doped zirconia with a tetragonal phase structure (t') as a secondary component for achieving high fracture toughness. Both the powders (c -phase) and (t' -phase) were manufactured by powder agglomeration and sintering processes, and then were mechanically blended into a composite phase powder ($c + t'$) with typical particle sizes of + 45–125 μm . The blending ratio of the two powders was determined based on a theoretical modeling of volumetric stacking for particle composites design, and was finally optimized based on the results of preliminary studies in thermal conductivity prediction and cyclic durability testing of the different blending powders and TBC samples. Figure 2 describes the model used for calculating volumetric stacking density for particle composites design, which is modified from the model similarly described (Ref 20). The key parameters include particle size, size distribution and spatial distances between particles.

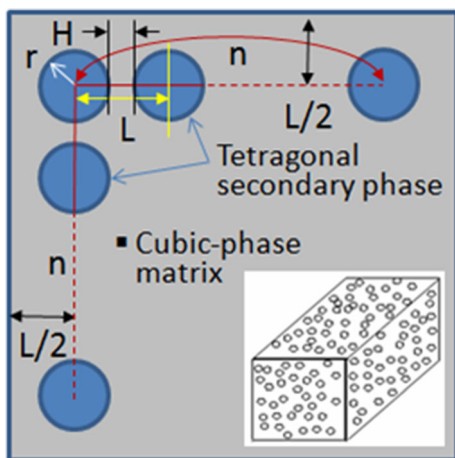


Fig. 2 Schematic of particle composite structure for theoretical calculation of secondary phase stacking density used in the phase composite TBC material design

Process Optimization and TBC Fabrication

Various TBC specimens were produced by Curtiss-Wright Surface Technologies (“CWST”) using a F4 plasma torch (Metco, Westbury, NY) for ceramic topcoats and a Jet Kote-3000 HVOF torch (Stellite, Goshen, IN) for a metallic CoNiCrAlY bondcoat (CO-210-24, Praxair) onto Haynes 188 substrates. A rough CoNiCrAlY flash layer over the dense alloy bondcoat was applied by HVOF process to improve the interface bonding between the bondcoat and the topcoat. An interlayer of *t'* phase zirconia as a compositional transition and strain buffer layer was deposited over the bondcoat prior to applying the composite phase topcoat. The spray parameters for the topcoat were experimentally investigated, optimized and determined primarily by the desirable targets on spray distance, feeding rate, coating porosity and deposition rate and efficiency. The composite phase low-*k* TBC with the optimized process has a porosity of 13~15% and a topcoat thickness of about 200 μm.

For comparison, several other types of TBC specimens also were prepared. They include composite phase low-*k* TBC with about 10% porosity (T-2, dense), single tetragonal phase TBC (T-3), single cubic phase TBC (T-4), and Gd₂Zr₂O₇ TBC (T-5, porosity: 10~12%. Powder source: Trans-Tech, Adamstown, MD). All the TBCs have an interlayer of *t'*-phase zirconia having a thickness of about 120 μm and porosity 10~12%. All the test TBC specimens are summarized in Table 1. The APS process efficiencies for ceramic topcoats were measured and compared among those coatings.

Table 1 List of types of TBC specimens used in this work

Specimen no.	Topcoat description	Porosity, %
T-1	<i>c</i> + <i>t'</i> phase zirconia (porous)	13-15
T-2	<i>c</i> + <i>t'</i> phase zirconia (dense)	8-10
T-3	<i>t'</i> phase zirconia	13-15
T-4	<i>c</i> phase zirconia	13-15
T-5	<i>p</i> phase Gd ₂ Zr ₂ O ₇ zirconate	10-12

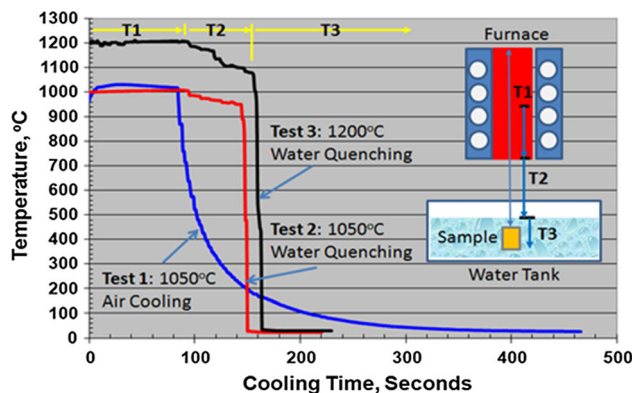


Fig. 3 Temperature profiles of rapidly thermal shock cyclic tests used for screening and evaluation of the cyclic resistance of the TBC specimens

Isothermal Oxidation Test

Isothermal oxidation test of the TBC specimens was conducted in air at 1300 °C. The specimens were placed in individual Al₂O₃ crucibles, and sequentially were located in the flat temperature zone of a Muffle box furnace with a temperature control accuracy of +/- 25 °C. At an interval of dwell time 20 to 25 h, some of the test samples were removed from the furnace, followed by cooling to room temperature and metallographic sectioning in a Metlab. The thickness of thermally grown oxide (TGO) scales in the sectioned specimens was measured, averaged and used to determine the TBCs’ oxidation kinetics. The oxidation test duration was accumulated for a total of 95 h at 1300 °C.

Thermal Shock Test

An internal procedure for rapidly thermal shock tests had been previously developed and performed mainly for the purpose of quick coating screening by comparing the various TBCs’ behavior of thermal shock response to aggressive rapidly cooling conditions (Ref 21). As depicted in Fig. 3, three types of thermal shock tests for all TBC specimens were performed by forced air cooling and water quench cooling from a holding temperature of 1050 or

1200 °C to near room temperature. For each thermal cycle, the test specimens were held at 1050 or 1200 °C with a dwell time of about 15 min, and then were removed from the furnace and were cooled rapidly by blowing the topcoat surfaces with a forced air or by dropping the specimens into a water container. After cooling to a stable temperature of about 25 to 45 °C, the test specimens were cleaned and or dried for visual surface inspection using a digital microscope. To determine the conditions of the TBCs underneath the topcoat surfaces, the top views of thermal images of the TBC samples at high temperatures were taken using an IR camera. After the visual inspection on the TBCs to detect visible coating damage or failure, the specimens were put back to the furnace to continue thermal cycling test until the completion of total 20 cycles of the standard thermal tests.

Sintering Test

The sintering behaviors of the TBCs were investigated isothermally at 1300 °C for the duration of 50 and 100 h without heating interruption, separately. With the same setup as the isothermal oxidation test, the TBC samples were placed in individual Al₂O₃ crucibles, and then were placed in the flat temperature zone in a Muffle box furnace with a temperature control accuracy of ± 25 °C. When holding time at temperature 1300 °C reached 50 or 100 h, the furnace was powered off and the samples were cooled slowly to room temperature inside the furnace. The sintered specimens were sectioned on the cross sections and examined in the changes of microstructures, phase structures, fracture morphologies, porosity and microhardness of the ceramic top layers.

Post-test Evaluation and Analysis

The as-sprayed and tested TBC samples were evaluated and analyzed using several Metlab technologies. The cross-sectional microstructures of the coating samples were observed mainly by means of an optical microscope and a scanning electron microscope (SEM). The fractured morphologies of the sintered TBC samples were examined closely at high magnitudes using SEM imaging method. The main chemical contents in the oxidized bondcoats were analyzed by energy-dispersive-x-ray spectroscopy (EDXS) equipped with the SEM. The TGO growth rates due to the oxidation exposure were estimated by measuring the thicknesses of the TGO layers in those TBC samples for different exposure dwell times. In conjunction with image analysis software, microstructure, cracking and porosity levels in the TBC coatings were characterized.

In addition, x-ray diffraction (XRD) for phase identification, phase quantity and lattice parameter measurement

was carried out using a computer-controlled diffractometer (MiniFlex 600, Rigaku, Tokyo, Japan), with CuK-alpha 0.154 nm radiation. The coating specimens were sectioned in a direction perpendicular to the coating plane and then metallographic specimens were prepared using a standardized grinding and polishing procedure. Then, microhardness HV300 was measured on the cross sections of the metallographic specimens using a microhardness tester.

Results and Discussion

Isothermal Oxidation TGO Behavior

In consideration of higher application temperatures for a low-*k* TBC, it is worthy to investigate its isothermal oxidation behavior at a higher temperature, specifically for the HVOF CoNiCrAlY bondcoat. The typical microstructures of the low-*k* TBC samples (T-1) are shown in Fig. 4. The three-layered microstructure consists of an alloy bondcoat,

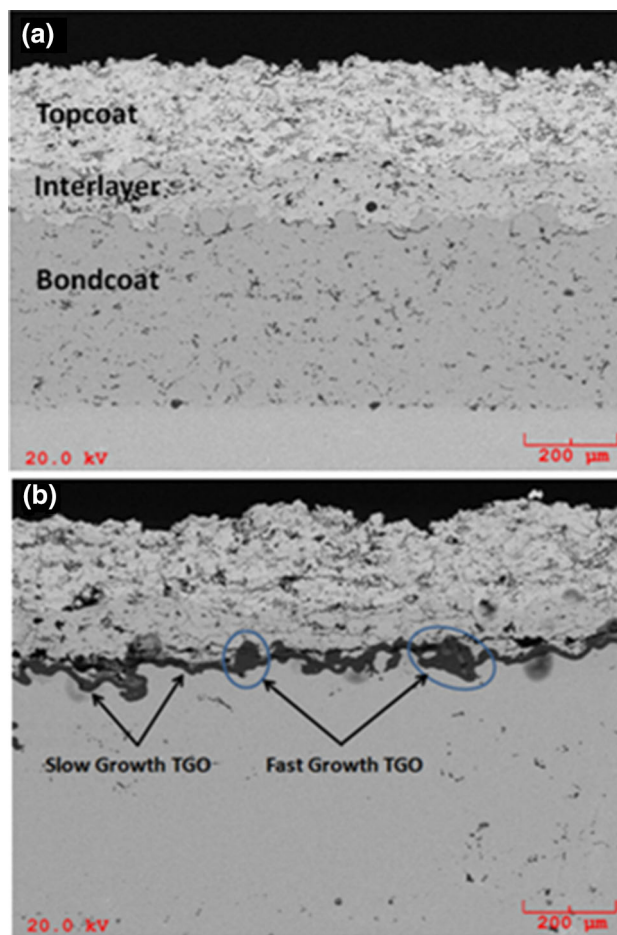


Fig. 4 SEM images of cross-sectional microstructures of the low-*k* TBC specimens (T-1): (a) As-sprayed, and (b) after oxidation test at 1300 °C

t'-phase zirconia interlayer and a *c + t'* composite phase low-*k* topcoat. The layers are well bonded at all the interfaces and are free of cracking. After thermally oxidized at 1300 °C, a dark and continuous TGO layer was formed over the bondcoat as shown in Fig. 4(b). By close observation, the TGO oxides can be divided into two groups based on TGO growth rates: (1) Group 1: slow growth TGO (S-TGO); (2) Group 2: fast growth TGO (F-TGO). The overall growth rates of the S-TGO and F-TGO are plotted with the square root of oxidation time $t^{1/2}$ in Fig. 5(a). The growth behavior of the S-TGO layer seems to have two stages, following a parabolic law as the test time increases. The growth rates of the S-TGO were calculated using the parabolic growth law, and the parabolic constants K_p were calculated using a linear data fitting method. It is obvious that the F-TGO grows much faster than the S-TGO in TGO thickness. The mode of multiple staged TGO growth with heat time is observed. For the initial 45 h of oxidation, both the TGOs gain their thickness at relative low rates, and then increase significantly. For the S-TGO growth, the first K_{S1} is calculated as

1.48 $\mu\text{m}/\text{h}^{1/2}$, and then, after 45 h the second K_{S2} increases to 4.68 $\mu\text{m}/\text{h}^{1/2}$. The K_{S2} value is consistent with the accelerated growth of the F-TGO simultaneously. Further analyzing the ratio of the F and S-TGOs in Fig. 5(b), it is revealed that the percentage of the S-TGO is dominant at near 95% for initial 45 h, but declines to about 70% at the end of the test. Accordingly, the percentage of the F-TGO increases from the initial 5 to 30%. Therefore, the critical thickness for the S-TGO growth can be derived as about 10 μm from the oxidation kinetic data. All the test specimens with different topcoats exhibited similar TGO growth modes.

To understand the TGO behavior, the analysis of element distribution mapping in the TGOs was performed using SEM/EDXS method. In Fig. 6, the distributions of key elements including O, Al, Cr, Fe, Co Ni and Zr are given. The S-TGO composes of pure $\alpha\text{-Al}_2\text{O}_3$ with minor amounts of elements Cr, Co and Ni. In contrast, the F-TGO is rich in elements Al, Cr, Co and Ni, indicating the formation of spinel type of oxides such as (Co, Ni) Al_2O_4 or mixture of spinel oxides, Cr_2O_3 and Al_2O_3 . Additionally, the analysis of chemical composition was performed in the bondcoats adjacent to the interface of the bondcoat and the TGO using SEM/EDXS method, and the results are summarized in Table 2. The result of very low Al content in the oxidized TBC sample indicates the degradation of $\beta\text{-NiAl}$ phase in the bondcoat to Ni_3Al and more likely γ phase due to the depletion of Al during the TGO growth and the interdiffusion between the bondcoat and the substrate at the high temperature (Ref 22). Based on the chemical analyses, it is believed that the K_{S1} and K_{S2} for the S-TGO growth should be correlated to the formation of pure $\alpha\text{-Al}_2\text{O}_3$ scale before the exposure of 45 h, and $\alpha\text{-Al}_2\text{O}_3 + \text{Cr}_2\text{O}_3$ mixed scale after the exposure of 45 h, respectively.

The microstructure of the oxidized bondcoat was further inspected by chemical etching and it was confirmed that all the NiAl phase in the bondcoat was depleted in the vicinity of the TGO interface. When the Al content is reduced to the minimum level (such as 4~5 wt.%), there is no sufficient Al source to support continuous and stable $\alpha\text{-Al}_2\text{O}_3$ (i.e., “good” S-TGO) growth, followed by the fast growth of non $\alpha\text{-Al}_2\text{O}_3$ (i.e., “bad” F-TGO) scale. Due to the test temperature exceeding the typical applied temperature of below 1100 °C for a MCrAlY-type bondcoat, the influence of the bondcoat degradation on long-term TBC lifetime and its chemical composition optimization needs to be further investigated to gain fundamental understanding for systematic design of a durable low-*k* TBC at higher temperature environments. As a whole TBC system, it is obvious that a high temperature capable bondcoat than regular HVOF MCrAlY-type bondcoat is necessary to be developed for a durable low-*k* TBC and the need toward prime reliant TBC.

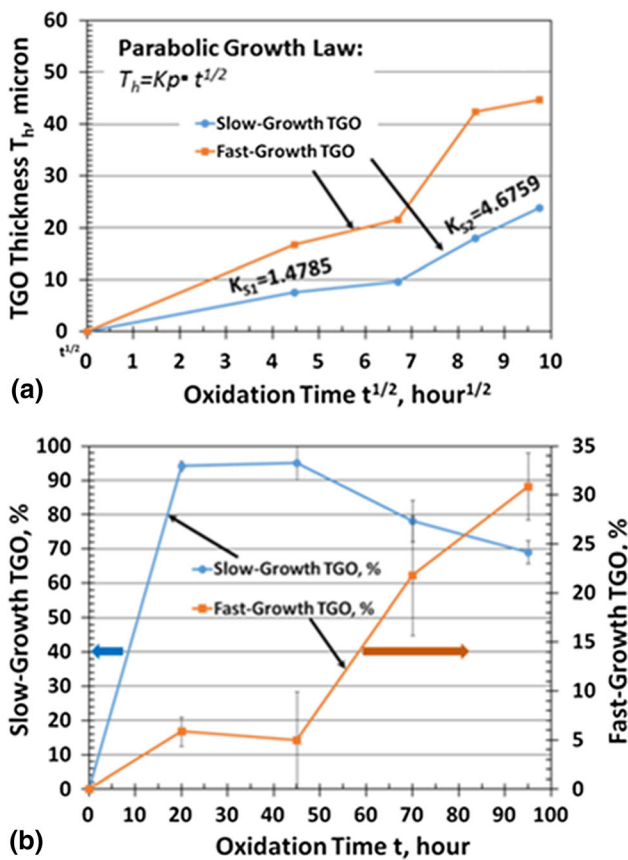


Fig. 5 Oxidation growth behavior of the TGO layer in the low-*k* TBC sample (T-1) at 1300 °C: (a) Plots of slow and fast TGO thicknesses with increasing oxidation time $t^{1/2}$ using linear fitting per parabolic growth law; (b) Percentages of the slow and fast TGOs vary with extending oxidation time *t*

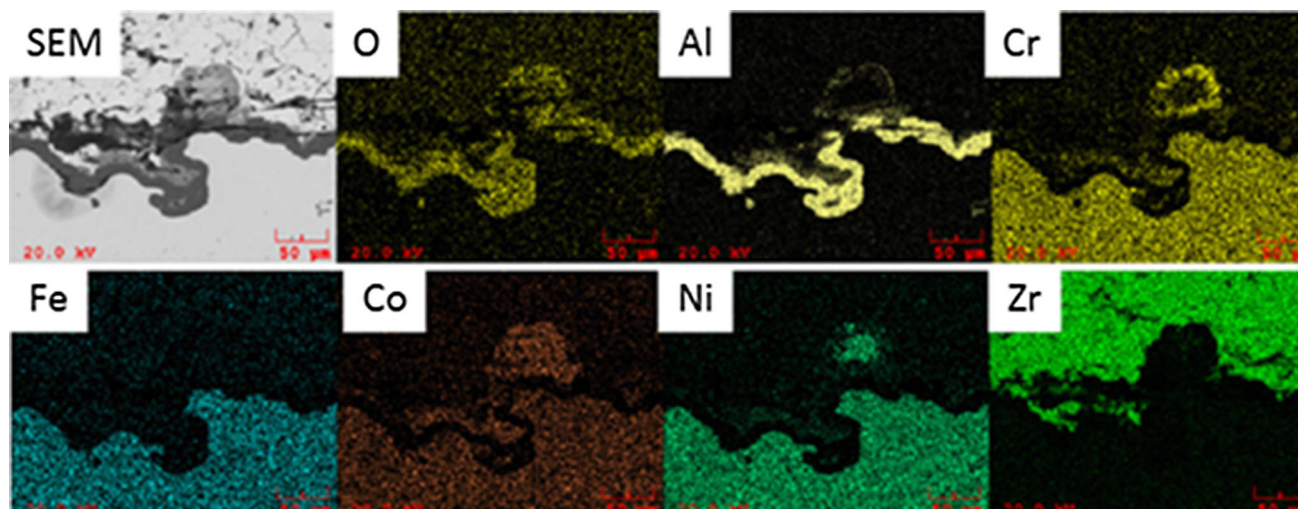


Fig. 6 SEM/EDXS mapping of key elements in the TGOs formed in the low- k TBC sample (T-1) after the oxidation test at 1300 °C in air

Table 2 Results of chemical composition analyses in as-sprayed and oxidized bondcoats (BC) in the low- k TBC (T-1)

Bondcoat description	Percentage of elements, wt.%			
	Al	Cr	Ni	Co
Key elements	Al	Cr	Ni	Co
Nominal BC powder	9	22	33	Balance
As-sprayed BC	10.4	20.8	32.4	Balance
Oxidized BC for 95 h	1.3	18.8	46	Balance

Table 3 Results of predicted thermal conductivity k for the low- k TBC specimen based on different models

Temperature	Thermal conductivity, W/m K		
	Maxwell–Garnett	Bruggeman	Linear mixing
1000 °C	0.83	0.83	0.83
1100 °C	0.88	0.88	0.89
1200 °C	1.10	1.10	1.11
1300 °C	1.16	1.16	1.17

Thermal Conductivity Prediction

The single phase zirconia-based ceramics and the APS-coatings with a cubic or tetragonal (prime) phase structure had been investigated extensively, and their thermal conductivity data were published or available as internal documentation (Ref 23–26). By utilizing available k data of the single phase materials, three theoretical methods for two-component ceramic composites were considered for predicting the thermal conductivity of the composite phase low- k TBC, with the nominal porosity 13 ~ 15%. The three models are described as below (Ref 27):

Method 1—Maxwell Garnett Model. In this model, k_1 and V_1 are the thermal conductivity and volume fraction of the continuous phase (i.e., c -phase low- k ceramic in this case), respectively, and k_2 and V_2 are the thermal conductivity and volume fraction of the dispersed phase (i.e., t' -phase ceramic in this case), respectively. The thermal conductivity k of the dual phase topcoat is given by Eq 1:

$$k = k_1 \left(\frac{k_2(1 + 2V_2) - k_1(2V_2 - 2)}{k_1(2 + V_2) + k_2(1 - V_2)} \right) \quad (\text{Eq 1})$$

Method 2—Bruggeman Model. The thermal conductivity of the dual phase topcoat is given by Eq 2:

$$V_1 \left(\frac{k_1 - k}{k_1 + 2k} \right) + V_2 \left(\frac{k_2 - k}{k_2 + 2k} \right) = 0 \quad (\text{Eq 2})$$

Method 3—Linear Rule of Mixture. The thermal conductivity of the dual phase topcoat is given by Eq 3:

$$k = k_1 V_1 + k_2 V_2 \quad (\text{Eq 3})$$

The thermal conductivity data derived from the three models are given in Table 3 for the temperature range of 1000 to 1300 °C. Among these three models, the k values from the methods 1 and 2 have very good agreement. The k values from method 3 deviate slightly from methods 1 and 2, but with < 1% variation. All the models are applicable to the case that each phase is contiguous and aligned parallel to the direction of heat flow and randomly dispersed phases with respect to the heat flow. In Table 3, the k values gain from 0.83 to 1.16 W/m K with increasing temperatures. By comparing with the k values of 8YSZ-TBCs (nominal 1.1 at 1000 °C, 1.2 at 1100 °C, 1.3 at 1200 °C and 1.4 W/m K at 1300 °C), the k values of the low- k ceramic are reduced by 15 ~ 27%, which is reasonable and agreeable to the experimental results in some related references (Ref 13, 23, 25). In conclusion, the three

theoretical models are introduced for thermal conductivity prediction of the two-phase composite and give very similar results. Further experimental investigation on thermal conductivity of the phase composite TBC is ongoing, and to be presented in future publication.

Thermal Shock Behavior

The TBC specimens listed in Table 1 were tested under three test conditions as given in Fig. 3. The results of visual inspection on the TBCs after the completion of thermal cyclic tests are summarized:

1. Test 1: Air cooling from heating temperature at 1050 °C. All the TBCs survived in the end of 20 cycles without coating delamination or spallation.
2. Test 2: Water cooling from heating temperature at 1050 °C. All the TBCs survived in the end of 20 cycles, except of that the zirconate TBC (T-5) has minor edge spallation of topcoat, total spallation area < 10% coating area.
3. Test 3: Water cooling from heating temperature at 1200 °C. The TBCs (T-1, T-2 and T-3) survived after 20 cycles with visible edge delamination. Their spallation areas are in the range of 7~19% total coating area, which is less than 30% defined as the threshold value for TBC failure. The TBCs (T-4 and T-5) failed due to the fact that their spallation areas are 39 and 43%, respectively, which are more than the threshold of 30%.

The visual inspection images of the TBCs after the 20-cycle thermal shock test by method 3 at 1200 °C are exhibited in Fig. 7. It was observed that the ceramic coatings T1, T2 and T3 delaminated locally on the edge areas, and there was no visible coating loss or cracking in the central coating areas. The edge coating spallation seemed to originate at the interface the bondcoat and the interlayer, and extend into the ceramic top layers. The infrared (IR) images confirmed no debonding of the ceramic layers in these TBCs. Furthermore, the percentages of the spalled areas were calculated using the image analysis method, and the results are given in Fig. 7.

The catastrophic ceramic topcoat failure was found on the TBC samples T-4 and T-5. The optical images demonstrated the loss of the ceramic materials happened on the coating edges and the central areas as well. The further inspection using the IR images indicated that the coating debonding and or lifting occurred in the ceramic topcoats, most likely near the interface of the interlayer and the bondcoat. Due to the existence of the inner delamination, the “true” values of the failed areas% were calculated using IR images. Obviously, the “true” values are larger

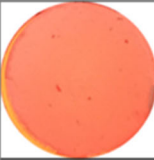
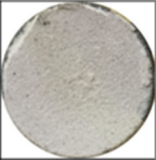
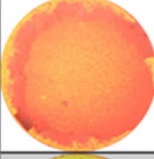
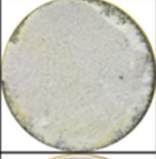
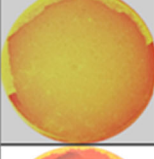
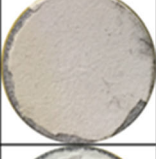
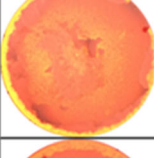
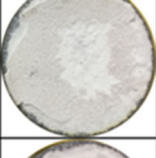
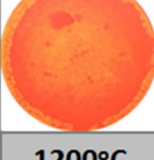
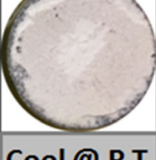
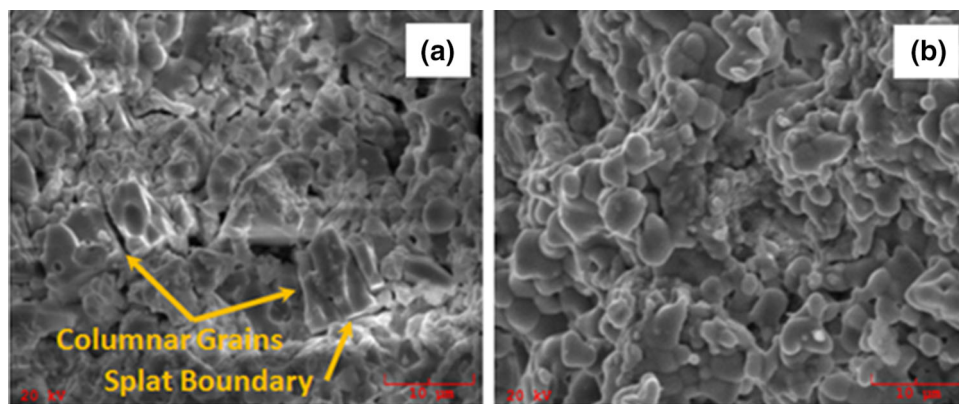
T-1			IR Image: 7% Optical: 7%
T-2			IR Image: 19% Optical: 19%
T-3			IR Image: 14% Optical: 14%
T-4			IR Image: 50% Optical: 39%
T-5			IR Image: 57% Optical: 43%
	1200°C	Cool @ R.T.	Spall Area

Fig. 7 Visual inspection images of the TBCs after 20-cycle thermal shock test by method 3 at 1200 °C. Left column: imaged by IR camera; Right column: by optical camera

than the “apparent” values derived from the optical images.

As expected, the more severe coating failure occurred when the higher heating temperatures and the more rapidly cooling condition was applied to those TBCs. One of the most interesting results is about the effect of t' -phase on thermal cycling behaviors of the TBC systems. All the samples containing partially or fully comprising of t' -phase in the ceramic topcoat had demonstrated superior thermal shock resistance relatively to the TBCs containing fully of cubic or pyrochlore phase. It is well known that t' phase zirconia has the highest fracture toughness at high temperature, however, cubic zirconia and pyrochlore zirconate has low fracture toughness (Ref 28). Among the specimens, the TBCs (T-1 & T-3) containing t' phase as well as a high coating porosity performed the best behavior due to outstanding thermal strain tolerance resulting from their improved fracture toughness. Therefore, those observations of the thermal shock tests confirmed that the design effectiveness of the composite phase low- k TBC by introduction of the secondary t' -phase into the cubic ceramic matrix. The effect of coating porosity on spallation behavior was noticed as well by comparing the TBC

Fig. 8 SEM fracture morphologies of the low- k TBC sample (T-1): (a) As-sprayed; (b) Sintered at 1300 °C/100 h



specimens between T-1 and T-2. It looks like the increase in coating porosity will be beneficial if merely considering of thermal shock resistance.

Sintering Behavior and Phase Stability

The topcoat of the as-sprayed low- k TBC (T-1) has a typically lamellar splat microstructure with some randomly distributed pores and microcracks, as presented in Fig. 8(a). After the sintering test at 1300 °C, the splats of the topcoat were sintered together and splat boundaries tended to disappear as shown in Fig. 8(b). Other distinct changes include the spheroidization and homogenization of lamellar grains and large pores, accompanying with microcrack healing and small-sized pore annihilation.

XRD spectra are presented in Fig. 9, covering 2θ ranges from 15° to 70°. Figure 9 shows that both non-transformable tetragonal (t') phase and cubic (c) phase are present in the feedstock powder and the as-sprayed topcoat. After sintering treatment, only t' and c phases were identified, without the evidence of phase transformation to a new monoclinic phase using software-based analyses. Therefore, the good thermal stability of the composite phase low- k coating is evident in the scan.

The microstructure of the sintered TBC (T-1) was examined, and several microstructural features were characterized by SEM image analyses. The main findings include: (1) The dispersive clusters comprising of agglomerated fine particles were sintered together dramatically, and resulted in the disappearance of the clusters and the pores within the clusters. (2) The large pores at inter-splat boundaries still existed or even became spherical and large. (3) Splat boundaries were quite distinct after sintering test, meaning no overall sintering took place, instead, sintering was limited in localized areas such as the agglomerated particle clusters, grain boundaries and within the individual splats as shown in Fig. 10.

To investigate the coating changes in physical properties, microhardness HV300 was measured on the cross

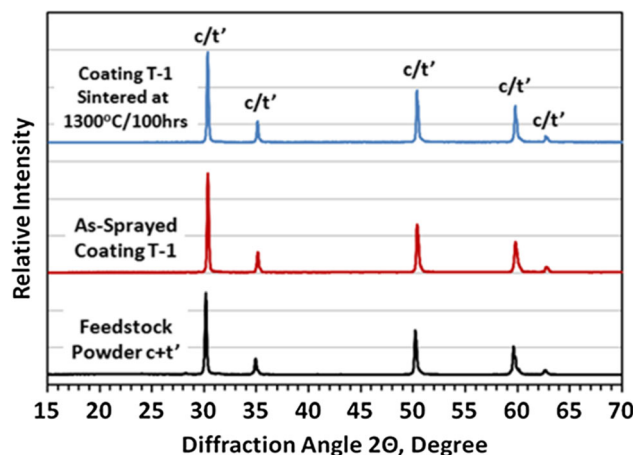


Fig. 9 XRD phase analyses of feedstock, as-sprayed and tested TBC samples

sections of the topcoats in the microstructural analysis samples. The HV300 value of the low- k TBC (T-1: $c + t'$ phase) is about 570 at the beginning and 779 after 100 h, increasing by 37%, as presented in Fig. 11. The TBC (T-3: t' phase) has increased HV300 from 607 to 949 by 56%, obviously more severely sintered than the composite phase TBC. Normally, sintering is considered as a kind of coating degradation and eventually is responsible for coating failure due to the loss of fracture toughness and strain tolerance of the ceramics (Ref 29, 30). With the aging and sintering of the TBCs, it is expected that a negative impact on thermal conductivity will happen, partially attributed to the coating densification. Based on the observation, inspection and analysis on the thermal behaviors of the tested TBCs, the composite phase low- k TBC exhibited its superiority in thermal stability, shock resistance and sintering resistance, showing its great potential and promising as a topcoat candidate with low- k capability and other desirable and vital property merits.

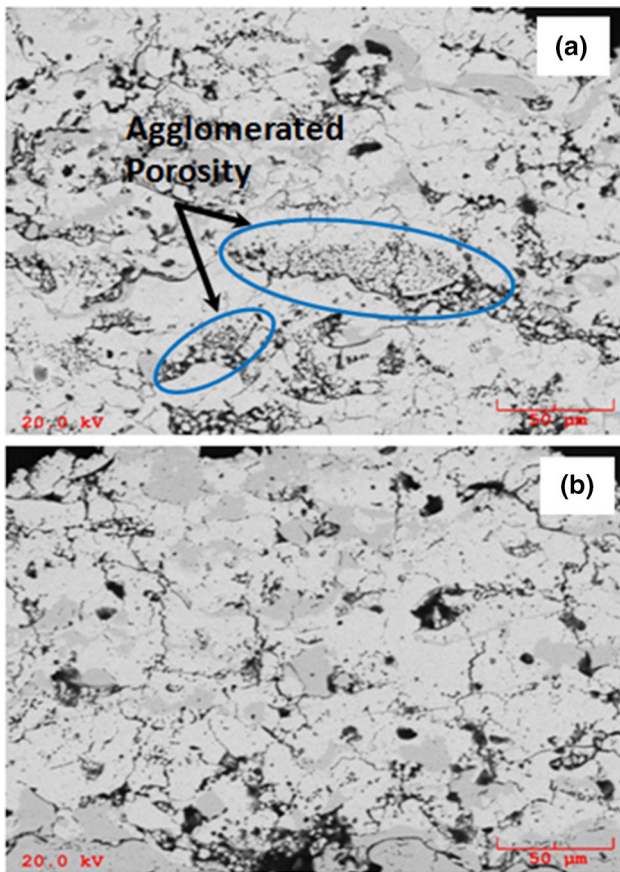


Fig. 10 SEM views of the cross-sectional microstructures of the low-*k* TBC T-1 samples: (a) As-sprayed; (b) After sintering test

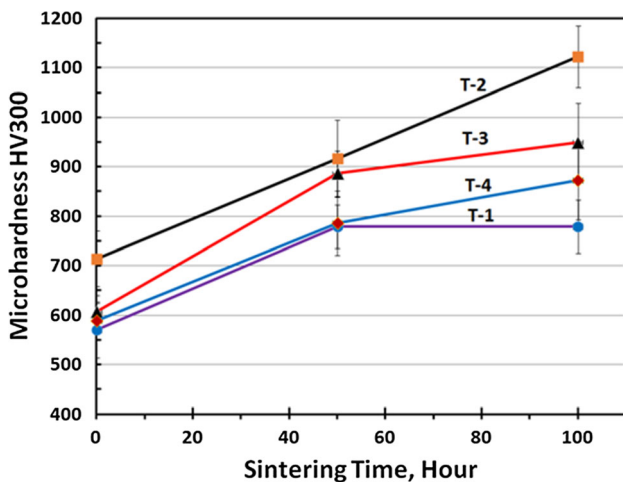


Fig. 11 Plots of microhardness HV300 with increasing time for those TBCs in sintering test at 1300 °C/50 and 100 h

Conclusions

The present work aimed to explore a path toward a durable TBC with low-*k* capability and improved thermal durability. The concept of composite phase composite ceramic

was adopted for low-*k* TBC material design, in an effort to combine the desirable property merits of unique dual phase constitution, low conductivity *k*, high ceramic fracture toughness and good process economy. The advantages of the composite phase (i.e., *c* + *t'*) TBC over single phase TBCs were demonstrated in the multiple tests:

1. The furnace isothermal oxidation test confirmed that both slow and fast growth TGOs were formed at 1300 °C. With prolonging the dwell time, the fast growth TGO dominated the oxidation behavior. The NiAl depletion in the bondcoat contributed to the increase in non-Al₂O₃ TGO and the deviation of TGO growth rate from a parabolic law.
2. The thermal shock tests under rapid cooling conditions showed that the TBCs containing tetragonal phase and high porosity exhibited greater thermal cycling durability based on the inspection on the damages and failure of the TBCs. The tetragonal phase component improved the strain tolerance of the low-*k* topcoats due to superior fracture toughness.
3. The sintering test at 1300 °C was performed to test the phase thermal stability and sintering behavior. The XRD results indicated that no phase transformation to monoclinic phase occurred in the low-*k* layer during the period of 100 h, but its densification was identified under the sintering condition.
4. All of the test specimens, the composite phase TBC exhibited the equivalent good thermal cycling resistance as the 8YSZ TBC, and was superior to c-phase zirconia and Gd₂Zr₂O₇ zirconate TBCs. The optimal behavior can be explained by the improved coating toughness from *t'*-8YSZ phase and the better thermal stability and less sintering from the c-zirconia phase in the composite phase low-*k* TBC.

Acknowledgments The authors gratefully acknowledge technical assistance and experimental support from Mr. David Reynolds, Development Engineering, Curtiss-Wright Surface Technologies, East Windsor, CT; and Mr. David Christie for SEM/EDXS analyses, IMR Test Labs, Curtiss-Wright Corporation, Lansing, NY.

References

1. D.R. Clarke and C.G. Levi, Materials Design for the Next Generation Thermal Barrier Coatings, *Ann. Rev. Mater Res.*, 2003, **33**, p 383-417
2. R. Vaßen, M. Jarligo, T. Steinke, D. Mack, and D. Stöver, Overview on Advanced Thermal Barrier Coatings, *Surf. Coat. Technol.*, 2010, **205**(4), p 938-942
3. J.H. Perepezko, The Hotter the Engine, the Better, *Science*, 2009, **326**, p 1068-1069
4. N. Curry, N. Markocsan, X. Li, A. Tricoire, and M. Dorfman, Next Generation Thermal Barrier Coatings for the Gas Turbine Industry, *J. Therm. Spray Technol.*, 2010, **20**, p 108-115

5. D.R. Clarke, M. Oechsner, and N.P. Padture, Thermal-Barrier Coatings for More Efficient Gas-Turbine Engines, *MRS Bull.*, 2012, **37**, p 891-898
6. S. Stecura, Effects of Compositional Changes on the Performance of a Thermal Barrier Coating System, *NASA TM-78976 Report*, (1978)
7. R.A. Miller, Thermal Barrier Coatings for Aircraft Engines: History and Directions, *J. Therm. Spray Technol.*, 1997, **6**(1), p 35-42
8. V.S. Stabican, Phase Equilibria and Metastabilities in the Systems ZrO_2 -MgO, ZrO_2 -CaO and ZrO_2 - Y_2O_3 , *Adv. Ceram.*, 1984, **24A**, p 71-85
9. D. Hasselman et al., Thermal Diffusivity & Conductivity of Dense Polycrystalline ZrO_2 Ceramics: A Survey, *Am. Ceram. Soc. Bull.*, 1987, **66**(5), p 799-806
10. K.W. Schlichting, N. Padture, and P.G. Klemens, Thermal Conductivity of Dense and Porous Yttria-Stabilized Zirconia, *J. Mater. Sci.*, 2001, **36**(12), p 3003-3010
11. D. Zhu and R.A. Miller, Thermal Conductivity and Sintering Resistance of Advanced Thermal Barrier Coatings, *Ceram. Eng. Sci. Proc.*, 2002, **23**, p 457-468
12. J.R. Nicholls, K.J. Lawson, A. Johnstone, and D.S. Rickerby, Methods to Reduce the Thermal Conductivity of EB-PVD TBCs, *Surf. Coat. Technol.*, 2002, **151–152**, p 383-391
13. X. Ma et al., Low Thermal Conductivity Thermal Barrier Coating Deposited by the Solution Plasma Spray Process, *Surf. Coat. Technol.*, 2006, **201**(7), p 4447-4452
14. R. Vassen, X. Cao, F. Tietz, D. Basu, and D. Stover, Zirconates as New Materials for Thermal Barrier Coatings, *J. Am. Ceram. Soc.*, 2000, **83**(8), p 2023-2028
15. D. Sedmidubsky, O. Benes, and R.J.M. Konings, High Temperature Heat Capacity of $Nd_2Zr_2O_7$ and $La_2Zr_2O_7$ Pyrochlores, *J. Chem. Thermodyn.*, 2005, **37**, p 1098-1103
16. W. Pan, S.R. Phillpot, C. Wan, A. Chernatynskiy, and Z. Qu, Low Thermal Conductivity Oxides, *MRS Bull.*, 2012, **37**, p 917-922
17. M.R. Winter and D.R. Clarke, Oxide Materials with Low Thermal Conductivity, *J. Am. Ceram. Soc.*, 2007, **90**(2), p 533-540
18. X.Q. Cao, R. Vassen, and D. Stoeber, Ceramic Materials for Thermal Barrier Coatings, *J. Eur. Ceram. Soc.*, 2004, **24**, p 1-10
19. R.M. Leckie, S. Krämer, M. Rühle, and C.G. Levi, Thermochemical Compatibility between Alumina and ZrO_2 - $GdO_{3/2}$ Thermal Barrier Coatings, *Acta Mater.*, 2005, **53**, p 3281-3292
20. O. Koutny, J. Kratochvil, J. Svec, and J. Bednarek, Modeling of Packing Density for Particle Composites Design, *J. Eur. Ceram. Soc.*, 1996, **18**(3), p 275-278
21. X. Ma and P. Ruggiero, *Cold Sprayed MCrAlY as a Bondcoat Candidate for TBC Application*, Long Beach, CA, May, Proc. Int. Therm. Spray Conf., 2015, p 20-26
22. Y. Tamarin, *Protective Coatings for Turbine Blades*, ASM International, Materials Park, 2006, p 79-96
23. D. Zhu and R.A. Miller, Thermal Conductivity of Advanced Ceramic Thermal Barrier Coatings Determined by a Steady-State Laser Heat-Flux Approach, *NASA/TM-2004-213040 Report*, ARL-TR-3262 (2004), p 1-18.
24. W. Chi and S. Sampath, Microstructure–Thermal Conductivity Relationships for Plasma-Sprayed Yttria-Stabilized Zirconia Coatings, *J. Am. Ceram. Soc.*, 2008, **91**(8), p 2636-2645
25. A.M. Limarga, S. Shian, M. Baram, and D.R. Clarke, Effect of High-Temperature Aging on the Thermal Conductivity of Nanocrystalline Tetragonal Yttria-Stabilized Zirconia, *Acta Mater.*, 2012, **60**, p 5417-5424
26. X. Ma et al., *Unpublished Report*, Curtiss-Wright Surface Technologies, East Windsor, 2017
27. J.P. Angle, Z. Wang, C. Dames, and M.L. Mecartney, Comparison of Two-Phase Thermal Conductivity Models with Experiments on Dilute Ceramic Composites, *J. Am. Ceram. Soc.*, 2013, **96**(9), p 2935-2942
28. E. Bakan and R. Vaßen, Ceramic Top Coats of Plasma-Sprayed Thermal Barrier Coatings: Materials, Processes, and Properties, *J. Therm. Spray Technol.*, 2017, **26**(6), p 992-1010
29. A. Keyvani, M. Bahamirian, and A. Kobayashi, Effect of Sintering Rate on the Porous Microstructural, Mechanical and Thermomechanical Properties of YSZ and CSZ TBC Coatings Undergoing Thermal Cycling, *J. Alloy. Compd.*, 2017, **727**, p 1057-1066
30. B. Lv et al., Sintering Resistance of Advanced Plasma-Sprayed Thermal Barrier Coatings with Strain-Tolerant Microstructures, *J. Eur. Ceram. Soc.*, 2018, **38**(15), p 5092-5100

Publisher's Note Springer Nature remains neutral with regard to jurisdictional claims in published maps and institutional affiliations.